Int. J. Heat Mass Transfer. Vol. 36, No. 2, pp. 411–422, 1993
Printed in Great Britain

0017-9310/93 $6.00 + 0.00

Pure material melting and solidification with liquid phase buoyancy and surface tension forces

A. LIU, T. E. VOTH and T. L. BERGMAN

Department of Mechanical Engineering, The University of Texas at Austin, Austin, TX 78712, U.S.A.

(*Received* 27 *December* 1991 *and in final form* 21 *February* 1992)

Abstract—Melting and solidification of pure materials, during which liquid convection is driven by buoyancy, or a combination of buoyancy and surface tension forces is considered. A numerical model, which is verified by comparing its predictions with experimental results, is used to show that thermocapillary effects can be of primary influence upon local melting rates in both relatively high and low *Pr* materials, and it can have a significant impact upon overall solidification. In low *Pr* materials, overall solidification rates are affected by thermocapillary convection more than overall melting rates. Thermocapillary convection is shown to have a significant influence upon phase change, regardless of the value of the dynamic Bond number considered in this study.

INTRODUCTION

CONSIDERABLE interest has developed regarding thermocapillary convection and its impact upon solid–liquid phase change during materials processing operations [1]. Despite the attention paid to surface tension phenomena, much remains to be learned of its interaction with buoyancy-induced convection during melting or solidification. For example, only qualitative experimental data exist which show the impact of surface tension driven convection on solid–liquid phase change. Analytical challenges are due, in part, to the presence of liquid domain boundaries (the solid–liquid interface as well as the liquid free surface) whose locations are not known beforehand. If surface tension forces become large relative to their viscous counterparts, oscillatory convection is established, further complicating experimentation and analysis [2, 3]. Surface chemistry associated with the presence of trace impurities within, or surfactants upon the melt can establish soluto- as well as thermocapillary forces which, in turn, alter liquid phase convection [4].

In this study, melting and solidification of low and moderately high *Pr*, nominally pure materials with convection driven by surface tension and buoyancy forces are considered. Hence this effort builds upon existing literature which deals with melting of low *Pr* materials [5, 6]. Because of the number of dimensionless parameters involved, selected results are presented for silicon, $Pr = 0.031$ [4], and sodium nitrate, $Pr = 9.25$ [7], the latter material having been used to mimic solidification of opto-electronic materials [8].

The model predicts phase change within the domain of Fig. 1. To preserve generality, a rectangular cavity with insulated top and bottom is considered. The vertical cavity walls are maintained at hot and cold temperatures inducing phase change at $S(y)$. The liquid free surface is subject to net horizontal surface tension forces comprised of soluto- and/or thermocapillary components which, along with thermal buoyancy forces, induce convection. In practice, solutal surface tension forces arise in nominally pure materials due to, for example, surface oxidation resulting from the material's exposure to trace amounts of air during processing. Solutocapillary forces oppose thermocapillary forces in most liquids.

Melting of solids at their fusion temperature is considered, while solidification proceeds numerically until a steady state is reached. Although the liquid's sensible energy and convective motion eventually subside in applications such as casting, it is maintained here by T_h in order to capture the phenomena relevant in, for example, melt growth and float zone growth or refinement of semiconductor crystals [4].

NUMERICAL MODEL

The melt free surface is assumed to be flat; an assumption which is strictly valid only when the contact angles at the cavity wall and solid are 90°, and at low *Ca*. The Boussinesq approximation is employed and the liquid's surface tension varies linearly with temperature. Viscous dissipation is ignored, as are the

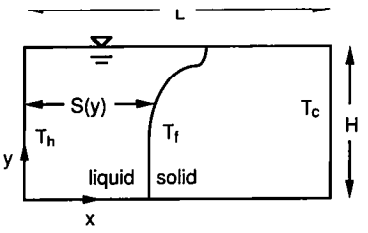

FIG. 1. The physical and coordinate systems.

NOMENCLATURE

A	aspect ratio, H/L
Bo	dynamic Bond number, Ra/Ma_T
c	concentration
Ca	capillary number, $\partial\sigma/\partial T \cdot \Delta T_l/\sigma$
D	surface concentration diffusion coefficient
$\mathbf{e}_\eta$	unit vector in η direction
Fo	Fourier number, $t \cdot \alpha_l/L^2$
g	gravitational acceleration
h	convection heat transfer coefficient, $-(k_l \partial T/\partial \mathbf{n})/(T_h - T_f)$
h_f	latent heat of fusion
H	enclosure height
k	thermal conductivity
k^*	thermal conductivity ratio, k_s/k_l
L	enclosure length
Le	Lewis number, α/D
Ma_c	solutal Marangoni number, $(\partial\sigma/\partial c)c_{avg}L/\mu_l \cdot \alpha_l$
Ma_T	thermal Marangoni number, $(\partial\sigma/\partial T)\Delta T L/\mu_l \cdot \alpha_l$
Nu	local Nusselt number at the solid–liquid interface, hL/k_l
$\overline{Nu}$	average Nusselt number at the hot wall, $\int_{\eta=0}^{A} Nu \cdot d\eta$ at $\xi = 0$
$\mathbf{n}$	normal unit vector
P	pressure
p	dimensionless pressure, $PL/\rho_l \cdot \alpha_l^2$
Pr	liquid Prandtl number, ν/α
Ra	liquid Rayleigh number, $g\beta\Delta T_l L^3/\nu_l \cdot \alpha_l$
s	dimensionless solid–liquid interface location, S/L
S	interface location
S_T	solid subcooling, $\Delta T_s/\Delta T_l$
Ste	liquid Stefan number, $c_l \cdot \Delta T_l/h_f$
t	time
T	temperature
ΔT	temperature difference, $T_h - T_f$ or $T_f - T_C$
$\mathbf{u}$	dimensionless velocity, UL/α_l
U	velocity
V	volume fraction
V_n	normal interface velocity
x	horizontal coordinate
y	vertical coordinate.

Greek symbols

α	thermal diffusivity
α^*	thermal diffusivity ratio, α_s/α_l
β	thermal expansion coefficient
η	dimensionless vertical coordinate, y/L, vertical control surface location
θ	dimensionless temperature, $(T - T_f)/\Delta T$
μ	dynamic viscosity
ν	kinematic viscosity
ξ	dimensionless horizontal coordinate, x/L, horizontal control surface location
ρ	density
ρ^*	density ratio, ρ_s/ρ_l
σ	surface tension
ψ	dimensionless streamfunction.

Subscripts and superscripts

c	concentration
C	cold
f	fusion
h	hot
i	solid–liquid interface, counter in the x direction
j	counter in the y direction
l	liquid
s	solid.

slight velocities normal to the interface induced by domain shrinkage and expansion. Radiation and convection interactions at the free surface are ignored and the liquid and solid are treated as radiatively opaque. The opacity assumption is suspect due to the thermally semitransparent nature of silicon and molten salts.

Upon incorporation of the assumptions, the governing equations are

liquid:

$$\nabla \cdot \mathbf{u} = 0 \tag{1}$$

$$\frac{\partial \mathbf{u}}{\partial Fo} + (\mathbf{u} \cdot \nabla)\mathbf{u} = -\nabla p + Pr\nabla^2 \mathbf{u} + Ra \cdot Pr \cdot \theta_l \mathbf{e}_\eta \tag{2}$$

$$\frac{\partial \theta_l}{\partial Fo} + \mathbf{u} \cdot \nabla \theta_l = \nabla^2 \theta_l \tag{3}$$

solid:

$$\frac{\partial \theta_s}{\partial Fo} = \alpha^* \nabla^2 \theta_s. \tag{4}$$

The initial conditions are

melting:

$$\text{at} \quad Fo = 0, \quad s = 0.01, \quad \theta_s = 0, \quad \theta_l = 1 \tag{5a}$$

solidification:

$$\text{at} \quad Fo = 0, \quad s = 0.99, \quad \theta_s = -1, \quad \theta_l = 1 \tag{5b}$$

while the boundary conditions are

$$\mathbf{u} = 0, \theta_l = 1 \quad \text{at } \xi = 0, \quad 0 \leqslant \eta \leqslant A \tag{6a}$$

$$\mathbf{u} = 0, \theta_s = 0 \text{ or } -1 \quad \text{at } \xi = 1, \quad 0 \leqslant \eta \leqslant A \tag{6b}$$

$$\mathbf{u} = 0, \partial\theta/\partial\eta = 0 \quad \text{at } \eta = 0, \quad 0 \leqslant \xi \leqslant 1 \tag{6c}$$

$$\mathbf{u} = 0, \partial\theta_s/\partial\eta = 0 \quad \text{at } \eta = A, \quad s \leqslant \xi \leqslant 1 \tag{6d}$$

$$\partial\theta_l/\partial\eta = 0 \quad \text{at } \eta = A, \quad 0 \leqslant \xi < s. \tag{6e}$$

The hydrodynamic boundary condition at $\eta = A$, $0 \leqslant \xi < s$ reflects the (potentially) simultaneous influences of surface thermal and concentration gradients [9]

$$\partial\mathbf{u}/\partial\eta|_{\eta=A} = Ma_T \cdot \partial\theta_l/\partial\xi|_{\eta=A} + Ma_c \cdot \partial C/\partial\xi|_{\eta=A} \tag{7}$$

in which the surfactant or oxidant concentration gradients are established along $\eta = A$ by combined one-dimensional advection and diffusion. As shown by the analysis and experimental results included and referenced in ref. [9], coupling between opposing solute- and thermocapillary surface tension forces establishes nearly stagnant conditions at the liquid free surface, regardless of the value of Le. In lieu of including surface chemical transport directly as in ref. [9], effective no-slip conditions, $\mathbf{u} = 0$ at $\eta = A, 0 \leqslant \xi < s$, are imposed and designated as the $Ma_c = \infty$ case. This approach implies that limiting case behavior ($Ma_c = 0$ or ∞) is to be predicted, and is taken solely to reduce the computational expense of the simulations. The coupling conditions at the solid–liquid interface are those associated with pure matter, since the surfactants or oxides are restricted to the free surface

$$\mathbf{u} = 0$$

$$\theta_s = \theta_l = 0$$

$$k^* S_T(\nabla\theta_s \cdot \mathbf{n}) - (\nabla\theta_l \cdot \mathbf{n}) = \rho^*/Ste \cdot V_n. \tag{8}$$

Results are presented in terms of the dimensionless streamfunction

$$\psi(\xi, \eta = 0) = \psi(\xi = 0, \eta = 0) - \int_0^\xi \mathbf{u}_\eta \, d\xi \tag{9}$$

$$\psi(\xi, \eta) = \psi(\xi, \eta = 0) + \int_0^\eta \mathbf{u}_\xi \, d\eta \tag{10}$$

where $\psi(\xi = 0, \eta = 0) = 0$, as well as the volume fractions of liquid

$$V_l = 1/A \int_0^A s \, d\eta \tag{11}$$

and solid, $V_s = 1 - V_l$. Heat transfer results (Nu and $\overline{Nu}$) are also reported. Note that the problem is governed by 11 dimensionless parameters (9 with the approximate treatment of solutocapillary effects).

Numerical procedure

The governing equations are solved numerically with a procedure nearly identical to that described in detail elsewhere [10]. In short, a nonorthogonal, curvilinear control volume-based methodology is used. All terms arising from the nonorthogonality are retained in the discretized equations, since curvature of the solid–liquid interface can be severe. Due to the costly nature of the simulations, the fully transient solution of ref. [10] is impractical, so the solid–liquid interface is advanced in a quasi-steady fashion. Upon convergence of the convection–diffusion equations (local mass residuals of less that 1×10^{-6} and energy balance achieved to within 0.1%), the solid–liquid interface is advanced.

An adaptive, nonuniform, nonorthogonal mesh is assigned to each phase with dense packing used at $\eta \approx A$, $\xi \approx s$ to resolve the severe local gradients [1]. Specifically

$$\xi_i = 1 - s(\xi, \eta) \cdot \left(\frac{i-1}{N}\right)^n \quad \text{for} \quad i = 1, 2, \ldots, N+1 \tag{12}$$

$$\eta_j = 1 - \left(\frac{j-1}{M}\right)^m \quad \text{for} \quad j = 1, 2, \ldots, M+1 \tag{13}$$

where $M = N = 38$, $m = n = 1.5$ (melting), $m = 1.75$, $n = 1.5$ (solidification). A grid network symmetric about $\xi = s$ is specified for $s < \xi \leqslant 1 - s$ while retaining the same η_j distribution as in the liquid phase.

The predictions are time step independent and are nearly grid independent. Grid independence was studied by performing preliminary simulations for a square liquid domain ($Ra = 7.5 \times 10^4$, $Ma_T = 4.4 \times 10^3$, $Pr = 9.25$) with 38×38 and 58×58 control volume meshes used. Local heat transfer rates differed by approximately 5% for the two simulations. The coarser mesh was used to obtain reasonably accurate solutions within reasonable computer time expenditures. Temporal resolution was determined for every case by halving the time step until differences between predictions could not be discerned. Here, $6 \times 10^{-9} \leqslant \Delta Fo \leqslant 4 \times 10^{-6}$. Solidification progressed numerically until steady state. Here, 99% of the local 'steady state' solid–liquid interface position is achieved within the first 75% of the simulation CPU time.

The simulations were performed on a battery of 10 IBM RS/6000 workstations. As is well known, accurate simulation of thermocapillary convection is expensive relative to buoyancy-driven flow. The $Ma_c = 0$ simulations required one to two orders of magnitude more CPU time using the same mesh and convergence criteria, under otherwise identical physical conditions as the buoyancy-driven flows considered here. Specifically, the thermocapillary simulations required a total CPU time of over 5000 h, making inclusion of fully transient, surfactant diffusion, three-dimensional and free surface deformation effects implausible.

RESULTS

Model validation

Quantitative experimental results for solid–liquid phase change have been obtained in an experimental

configuration consistent with the geometry of Fig. 1 [11, 12]. Included in ref. [13] are detailed descriptions of the experimental techniques, procedures and estimated uncertainties, as well as a listing of the thermophysical properties of the test liquid (silicone oil) and solid (ice). Note that $H = 20$ mm in the experiments.

Figure 2 includes results for a conjugate experiment at steady state ($A = 0.5$, $Ra = 32\,000$, $Ma_T = 1500$, $Ma_c = 0$, $Ste = 0.047$, $S_T = 0.35$ and $Pr = 1755$). Shown are the observed streamline distribution (Fig. 2(a)) and the measured liquid surface temperature distribution (Fig. 2(b)). Note that the actual liquid phase free surface and solid–liquid interface reflect the streamline image of the liquid phase, whose ultimate size and shape is determined by a balance of liquid and solid phase heat transfer at the solid–liquid interface. The predicted liquid phase domain is shown in Fig. 2(c), along with the observed domain whose solid–liquid interface is indicated by the dashed line and whose center of rotation is shown by the cross. Excellent agreement is noted between the experimental results and numerical predictions.

Relatively high surface velocities advect warm fluid into the upper right portion of the liquid domain (Fig. 2(d)) leading to high local heat transfer to the solid–liquid interface. The predicted liquid surface temperature and horizontal velocity distributions are also shown in Fig. 2(b). Since silicone oil is not susceptible to solutocapillary forces, predictions using the no-slip surface condition are in poor agreement with the experimental results [12].

Figure 3 shows the observed and predicted liquid phase domains and streamline distributions for a melting experiment ($A = 0.5$, $Ra = 32\,000$, $Ma_T = 1500$, $Ma_c = 0$, $Ste = 0.047$, $S_T = 0$ and $Pr = 1755$). Predicted liquid temperature distributions are also shown. Thermal buoyancy and surface tension forces combine to induce liquid convection, with thermocapillary forces inducing large surface velocities and propagation of warm liquid from left to right, enhancing melting in the upper portions of the domain. Note that the experimental center of rotation is shown by a cross superposed upon the predicted streamline distribution. Predictions using the effective no-slip condition at the free surface are in poor agreement with the experimental results [12].

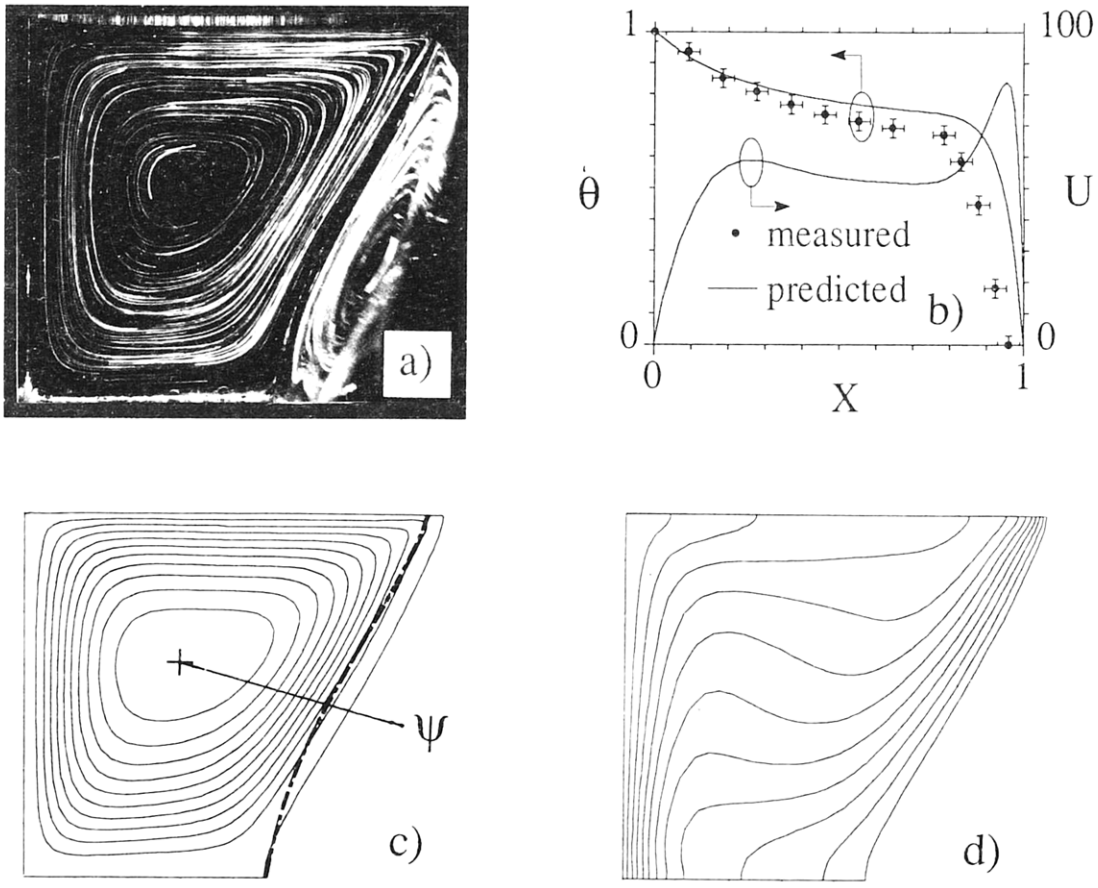

FIG. 2. Comparison of measured and predicted results including: (a) the observed liquid phase domain and streamlines, (b) measured and predicted surface temperature and predicted velocity distributions, (c) the predicted liquid phase domain size and streamlines ($\psi = -9.66$), and (d) the predicted liquid phase temperature distribution.

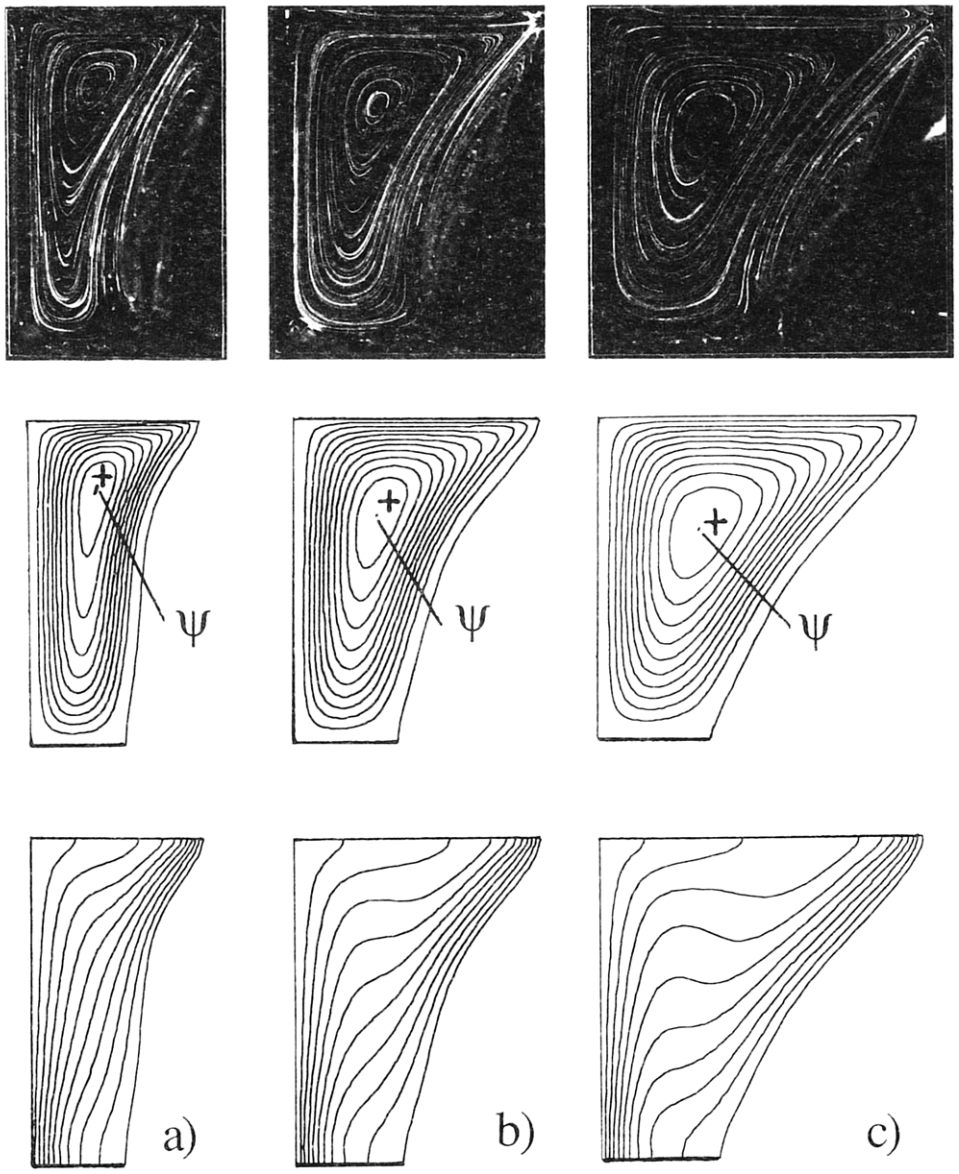

FIG. 3. Observed (top row) and predicted (middle and bottom rows) liquid phase convection during melting of ice with silicone oil. The predictions are for: (a) $Fo = 2.4$, $\psi = -4.96$, (b) $Fo = 4.8$, $\psi = -6.91$, and (c) $Fo = 8.0$, $\psi = -8.57$.

Based upon the agreement of the predictions with experimental data, the model is considered to be validated. Melting and solidification of low and relatively high Pr materials are considered next, and the dimensionless parameters are shown in Table 1. The Ra, $Ma_{T,c}$, Ste and S_T values are associated with melting or solidification of pure silicon with $H = 5$ or 20 mm and $T_h - T_f = 10$ C. Note that Ra and Ma values are different for the melting and solidification cases because of the different aspect ratios used (Ra and Ma based on H are identical). Thermophysical properties are listed in Table 2.

Melting

Figure 4 shows the liquid phase for silicon (Figs. 4(a)–(c)) and sodium nitrate (Figs. 4(d)–(f)) for $Ma_c = 0$, $Ra = 6.75 \times 10^5$ and $Ma_T = 1.32 \times 10^4$. The liquid domains shown are of identical volume fractions, specifically $V_l = 0.107$ in Figs. 4(a) and (d), $V_l = 0.173$ in Figs. 4(b) and (e), while $V_l = 0.327$ in Figs. 4(c) and (f). Figure 5 includes predicted Nu corresponding to the results of Fig. 4, as well as for associated $Ma_c \approx \infty$ simulations.

For either material, melting is most rapid at $\eta \approx A$. Also, the major center of rotation, ψ_1, propagates downward with time, reflecting the increasing strength of buoyancy relative to thermocapillary forces as the liquid phase expands. Detailed descriptions of the low Pr behavior are available in refs. [5, 6] and only pertinent features are noted here. Specifically, the silicon is characterized by multi-cellular convection with an upper cell driven primarily by thermocapillary forces

Table 1. Dimensionless parameters associated with the parametric simulations

Case	Pr	Ra	Ma_T	Ma_c	A	Ste	S_T	Bo
				Melting				
1	0.031	6.75×10^5	1.32×10^4	0, ∞	1/3	5.14×10^{-3}	0	51.1
2	0.031	1.05×10^4	3.27×10^3	0, ∞	1/3	5.14×10^{-3}	0	3.21
3	9.25	6.75×10^5	1.32×10^4	0, ∞	1/3	4.95×10^{-2}	0	51.1
4	9.25	1.05×10^4	3.27×10^3	0, ∞	1/3	4.95×10^{-2}	0	3.21
				Solidification				
5	0.031	2.00×10^5	8.80×10^3	0, ∞	1/2	5.14×10^{-3}	2.5, 4.0	22.7
6	0.031	3.11×10^3	2.18×10^3	0, ∞	1/2	5.14×10^{-3}	2.5, 4.0	1.43
7	9.25	2.00×10^5	8.80×10^3	0, ∞	1/2	4.95×10^{-2}	2.5, 4.0	22.7
8	9.25	3.11×10^3	2.18×10^3	0, ∞	1/2	4.95×10^{-2}	2.5, 4.0	1.43

Table 2. Thermophysical properties of sodium nitrate and silicon

Property	$NaNO_{3_l}$	$NaNO_{3_s}$	$silicon_l$	$silicon_s$
ρ (kg m^{-3})	1904 [7]	2261 [14]	2520 [4]	2302 [18]
ν (m^2 s^{-1})	1.46×10^{-6} [7]	—	3.97×10^{-7} [4]	—
c (J kg^{-1} K^{-1})	1880 [7]	1823 [15]	930 [4]	1000 [18]
k (W m^{-1} K^{-1})	0.565 [7]	0.588 [16]	30.0 [4]	22.0 [18]
α (m^2 s^{-1})	1.58×10^{-7}	—	1.28×10^{-5}	—
$\partial\sigma/\partial T$ (N m^{-1} K^{-1})	-7.0×10^{-5} [14]	—	-2.79×10^{-4} [17]	—
h_f (kJ kg^{-1})	—	182.3 [16]	—	1808 [18]
β (K^{-1})	6.6×10^{-4} [14]	—	2.0×10^4 [4]	—
Pr	9.25	—	0.031	—

and a bottom rotation (Fig. 4(a)) induced by buoyancy. A middle cell (ψ_2) is driven by shear interaction with its neighbors. At early times the buoyancy-induced flow is of sufficient strength to advect warm temperatures to the solid–liquid interface at $\eta/A \approx 2/3$, resulting in enhanced melting locally (Fig. 4(a)). With time, the top and bottom cells merge (Fig. 4(b)), with a smaller cell (ψ_2) located beneath the lip of the solid–liquid interface which is pushed downward with time (Fig. 4(c)). The buoyancy-affected local melting is not evident at later times, with $S(y)$ increasing monotonically with y.

The Nu distributions of Fig. 5(a) are characterized by local maxima and minima traceable to the multicellular convection and relatively complex liquid phase domain of Figs. 4(a)–(c). At $Fo = 0.95$, for example, buoyancy is of sufficient strength to induce high local heat transfer rates in the range $0.3 \leqslant \eta/A \leqslant 0.7$. Minimum Nu exist at $\eta/A \approx 0.8$ and are associated with the cool fluid trapped within ψ_2 of Fig. 4(a). Maximum Nu exist at $\eta/A \approx 0.85$ and are associated with the impingement of downflow within the thermocapillary cell upon the solid protruding into the liquid domain. The largest Nu occur near $\eta/A = 1$. As time progresses, the complexities of the Nu distribution are reduced since the vigorous buoyancy-induced convection cell merges with the thermocapillary-driven cell, resulting in the relatively straightforward Nu distribution of $Fo = 5.64$. Even at the latest time shown, however, minimum Nu exist near $\eta/A = 0.20$ due to the recirculation, ψ_2, of Fig. 4(c). The Nu distributions associated with $Ma_c = \infty$ are as expected, and Nu locally exceeds that of $Ma_c = 0$ in the lower portions of the liquid domain.

Sodium nitrate (Figs. 4(d)–(f)) is characterized by unicellular convection throughout the melting process (except for the initial stages, $Fo \leqslant 0.1$). As expected, the higher Pr liquid's heat transfer is affected by convection more than the silicon, with its free surface length exceeding that of the silicon (for equal V_1) throughout time. Here, thermocapillary effects are considered to be more vigorous than for silicon in the sense that the center of rotation is confined to large η/A and the liquid free surface is large. Since Pr is high, surface temperature gradients near the solid–liquid interface are large relative to the silicon, increasing the thermocapillary component of equation (7) directly.

Large Nu (Fig. 5(b)) exist at the free surface and, as in the silicon, above the protruding solid in the location of the thermocapillary-induced downflow. Minimum Nu, attributed to ψ_2 in the silicon, are nonexistent for the sodium nitrate. As in the silicon, heat transfer rates associated with the $Ma_c = \infty$ simulation can be decreased in the bottom portions of the liquid layer due to the role of thermocapillary convection in restricting the most vigorous convective activity to regions near the free liquid surface and, in turn, inducting a relatively strong return flow from the cold solid toward the hot wall at intermediate η/A.

Similar trends regarding the liquid phase dynamics and local convective heat transfer rates are noted for the low Ra_T, Ma_T simulations [11]. The no-slip predictions of the liquid phase hydrodynamics are well

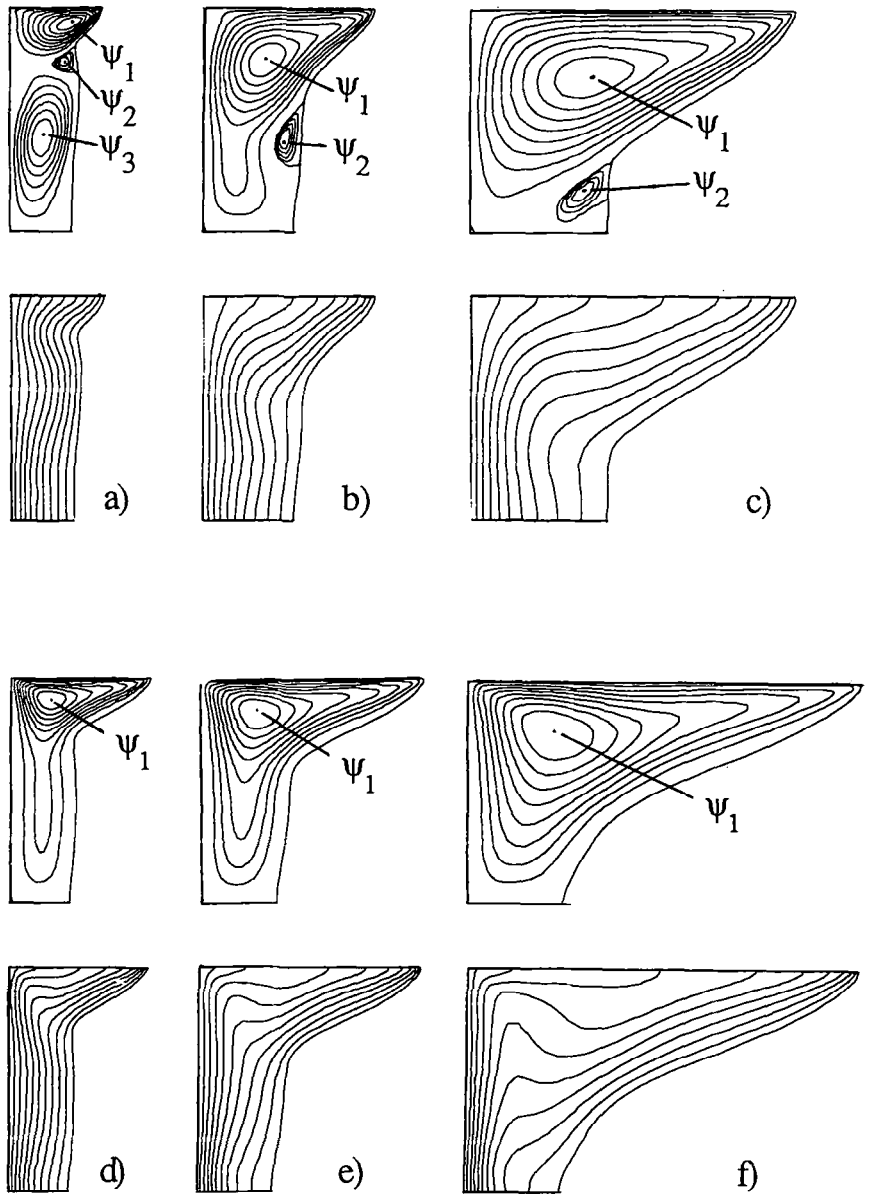

FIG. 4. Predicted liquid phase convection during melting of silicon at: (a) $Fo = 0.95$, (b) $Fo = 2.23$, (c) $Fo = 5.64$ and sodium nitrate, (d) $Fo = 0.11$, (e) $Fo = 0.23$, and (f) $Fo = 0.50$. Streamfunction values are: (a) $\psi_1 = -2.01$, $\psi_2 = 0.10$, $\psi_3 = -1.54$, (b) $\psi_1 = -3.53$, $\psi_2 = 0.08$, (c) $\psi_1 = -4.89$, $\psi_2 = 0.08$, (d) $\psi_1 = -6.29$, (e) $\psi_1 = -8.74$, (f) $\psi_1 = -12.90$.

understood and bear only modest resemblance to those shown here (as implied by the $Ma_c \approx \infty$, Nu distributions shown in Fig. 5). As expected, smaller Nu are predicted for the silicon relative to the higher Pr sodium nitrate [11].

Instantaneous solid–liquid interface locations for both materials (including $Ma_c \approx \infty$) are shown in Fig. 6. Thermocapillary effects are significant, even for relatively large physical systems (large Bo) involving low Pr liquids (Fig. 6(a)). Melting at low Ra (Figs. 6(b) and (d)) becomes convection dominated when thermocapillary forces are not offset by solutocapillary effects. The inclusion of thermocapillary forces yields decreased melting rates at locations far from the free surface, as a consequence of the interplay between buoyancy and thermocapillary forces throughout the liquid region.

Overall melting rates may be inferred from the $\overline{Nu}$ history shown in Fig. 7. The overall silicon melt rate (Figs. 6(a), 7(a) and 6(b), 7(b)) is relatively insensitive to thermocapillary effects, even though liquid phase convection augments localized melting significantly at high Bo (Figs. 6(a), 7(a)). This insensitivity is due to the offsetting enhancement and reduction in local melting induced by multi-cellular convection evident in Figs. 6(a) and (b). In contrast, the sodium nitrate

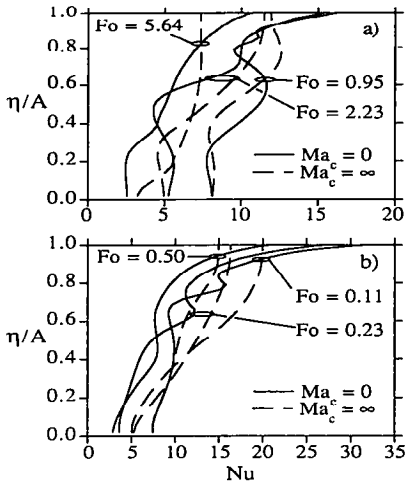

FIG. 5. Predicted *Nu* for the times shown in Fig. 4. Results are for: (a) silicon and (b) sodium nitrate. Effective no-slip and thermocapillary predictions are shown by the dashed and solid lines, respectively.

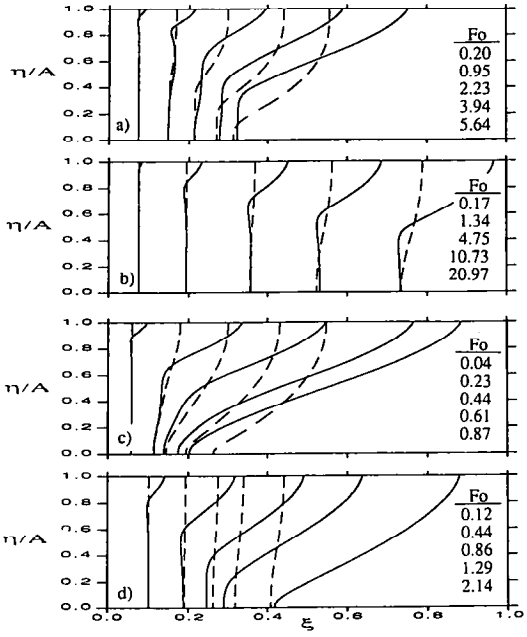

FIG. 6. Selected solid–liquid interface locations during melting. No-slip and thermocapillary results are shown by the dashed and solid lines, respectively. The predictions for Simulations 1–4 are shown in (a)–(d) respectively.

melting rate is augmented significantly by thermocapillary forces (Figs. 6(c), 7(c) and 6(d), 7(d)). Early transition to convectively dominated melting is promoted by thermocapillarity, as evidenced by the departure from the conduction solution for all of the cases relative to the $Ma_c = \infty$ results. For the low *Bo*, moderate *Pr* case (Figs. 6(d) and 7(d)) melting may be mistakenly deemed conduction dominated, if thermocapillary effects are neglected. Note that thermocapillary effects can lead to an increase in $\overline{Nu}$ with time (Fig. 7(c)) in contrast to the relatively constant $\overline{Nu}$ histories of buoyancy-induced melting [19].

Solidification

Surface tension phenomena are also present during solidification, but, since the solid phase conduction is

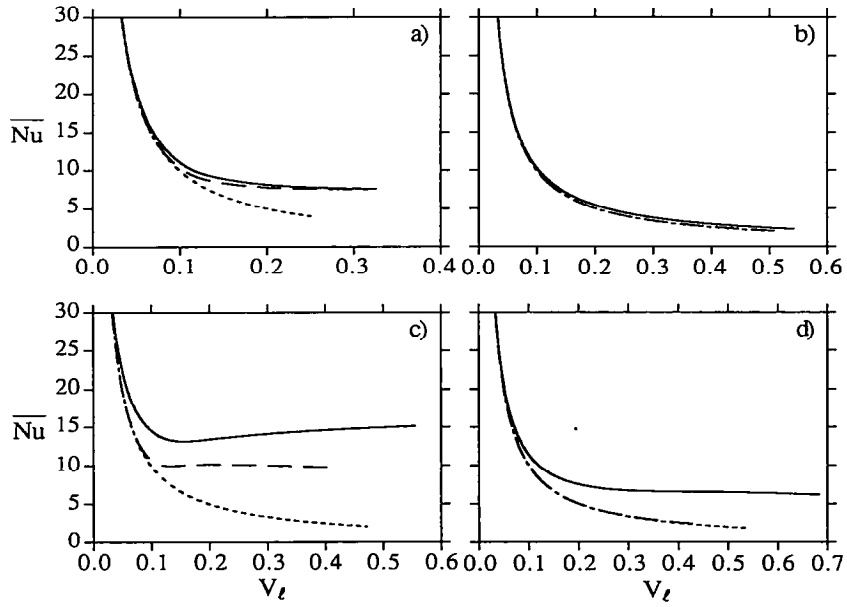

FIG. 7. Predicted $\overline{Nu}$ histories during melting. Results are for: (a) silicon, *Bo* = 51.1, (b) silicon, *Bo* = 3.21, (c) sodium nitrate, *Bo* = 51.1, (d) sodium nitrate, *Bo* = 3.21. The distributions are for the conduction solution (short dashed line), the no-slip simulation (large dashed line) and the thermocapillary simulation (solid line).

important in the solid–liquid interface energy balance (equation (8)), the impact of surface tension may be less than during melting. The degree of solid phase subcooling (S_T) may impact on the thermocapillary's relative influence upon solidification.

Figure 8 shows liquid (convective) heat transfer characteristics for the low and high Pr materials at low Bo and high S_T. The liquid domains shown are of identical volume fractions, specifically $V_l = 0.675$ in Figs. 8(a) and (d), $V_l = 0.362$ in Figs. 8(b) and (e),

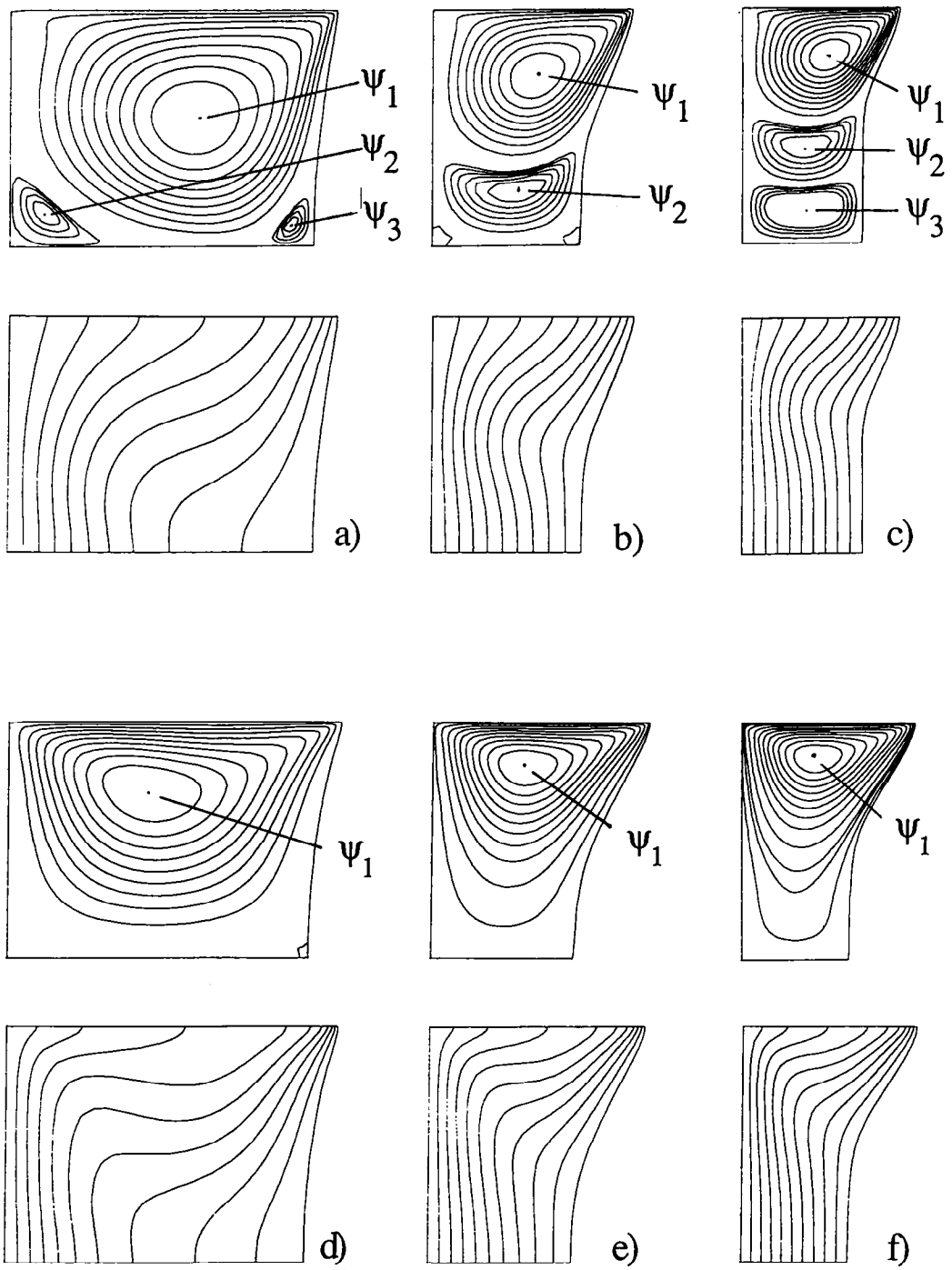

FIG. 8. Predicted liquid convection during solidification of silicon at: (a) $Fo = 3.84$, (b) $Fo = 24.3$, (c) $Fo = \infty$ and sodium nitrate, (d) $Fo = 0.39$, (e) $Fo = 2.14$ and (f) $Fo = 3.90$. For all cases, $Bo = 1.43$ and $S_T = 4.0$. Streamfunction values are: (a) $\psi_1 = -2.87, \psi_2 = 0.036, \psi_3 = 0.035$, (b) $\psi_1 = -2.02, \psi_2 = 0.087$, (c) $\psi_1 = -1.79, \psi_2 = 0.087, \psi_3 = -0.02$, (d) $\psi_1 = -5.75$, (e) $\psi_1 = -4.26$, (f) $\psi_1 = -3.68$.

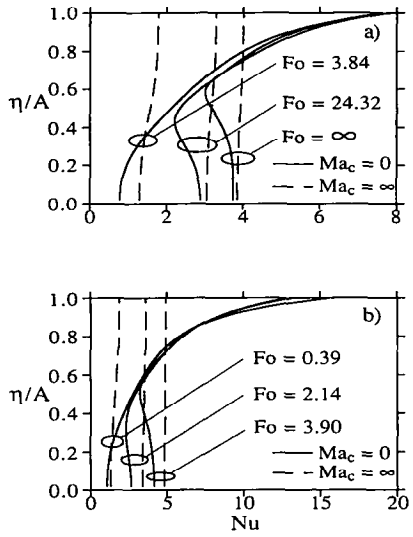

FIG. 9. Predicted *Nu* for the times shown in Fig. 4. Results are for: (a) silicon and (b) sodium nitrate. Effective no-slip and thermocapillary predictions are shown by the dashed and solid lines, respectively.

while $V_1 = 0.277$ in Figs. 8(c) and (f). In a manner similar to low *Bo* melting cases [5, 11], the silicon is characterized by multi-cellular convection at smaller liquid fractions, while a vigorous thermocapillary-driven cell is present for large liquid fractions. The multi-cellular structure in Fig. 8(c) consists of a top thermocapillary driven circulation, a bottom buoyancy driven circulation and an intermediate counter-rotating cell. In contrast to the silicon, the sodium nitrate is characterized by unicellular convection throughout solidification.

Significant variations in *Nu* exist along the solid–liquid interface, and specific results are shown in Fig. 9. As in melting, heat transfer enhancement occurs near the liquid surface for $Ma_c = 0$. In contrast to the results of Fig. 4, the complexity of the liquid domain's shape is modest, and local solid protrusions into the liquid domain are slight. As such, heat transfer modification due to impingement of the thermocapillary flow upon the protruding solid phase is not important. Multi-cellular convection still exists within the low *Pr* silicon, however, and variations in *Nu* are attributed

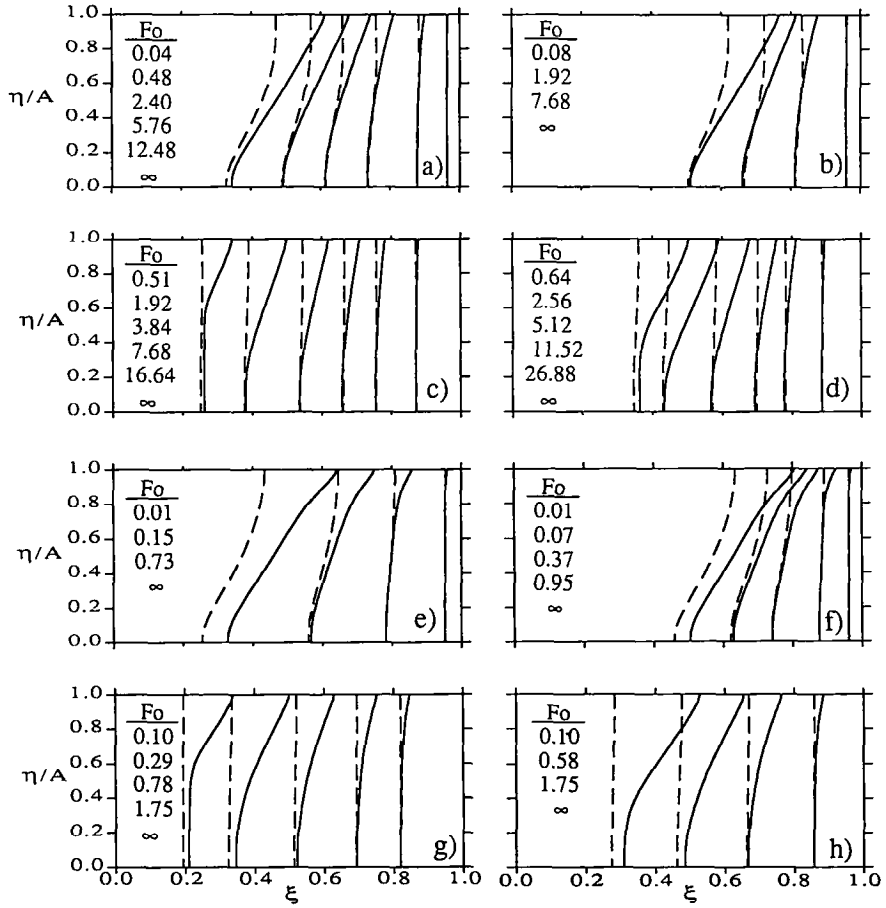

FIG. 10. Predicted solid–liquid interface locations during solidification. Effective no-slip and thermocapillary simulated interface positions are shown by the dashed and solid lines, respectively. The predictions are for Simulation 5 (a) and (b), Simulation 6 (c) and (d), Simulation 7 (e) and (f) and Simulation 8 (g) and (h). The high S_T results are in the left panel.

to its presence. In the high Pr silicon nitrate (Fig. 9(b)) local Nu variations are modest in the lower portions of the liquid, suggesting little influence of either multicellular convection or geometrical complexity upon convection. In either material, the low Nu for $\eta/A \leqslant 0.5$ is due to thermocapillary's role in confirming the most vigorous convection in the upper part of the liquid domain. At low Bo, the $Ma_c \approx \infty$, Nu distributions are conduction dominated.

Predicted solid–liquid interface locations during solidification are shown in Fig. 10. In each case, the interface propagates from right to left, and the far left results are associated with the steady state. As in Fig. 6, a comparison is made with predictions using no-slip hydrodynamic boundary conditions. As required and expected, more material solidifies as S_T is increased, and the higher Nu near $\eta = A$ leads to decreased solidification at that location. Solidification at low Bo, $Ma_c \approx \infty$ is conduction dominated.

In contrast to the $Ma_c = 0$ results of Fig. 6, in which enhanced local melting rates near the free surface are offset by local decreases elsewhere (leading to an insensitivity of overall melting rates to thermocapillary convection in low Pr materials, Fig. 7), solidification rates are decreased everywhere along the solid–liquid interface. This behavioral difference is attributed to (i) the relative sizes of the liquid regions associated with melting and solidification and (ii) solid phase conduction during solidification. Specifically, the relatively large liquid volume fractions of Fig. 10 allow thermocapillary effects to propagate further downward into the liquid phase. As a result, the sharp Nu variations associated with melting are smoothed, as was evident in Fig. 9. Furthermore, solid phase conduction desensitizes the system response to variations in Nu with, for example, the high convective heating near $\eta/A = 1$ offset by high diffusive cooling at the same location. Because of these differences dur-

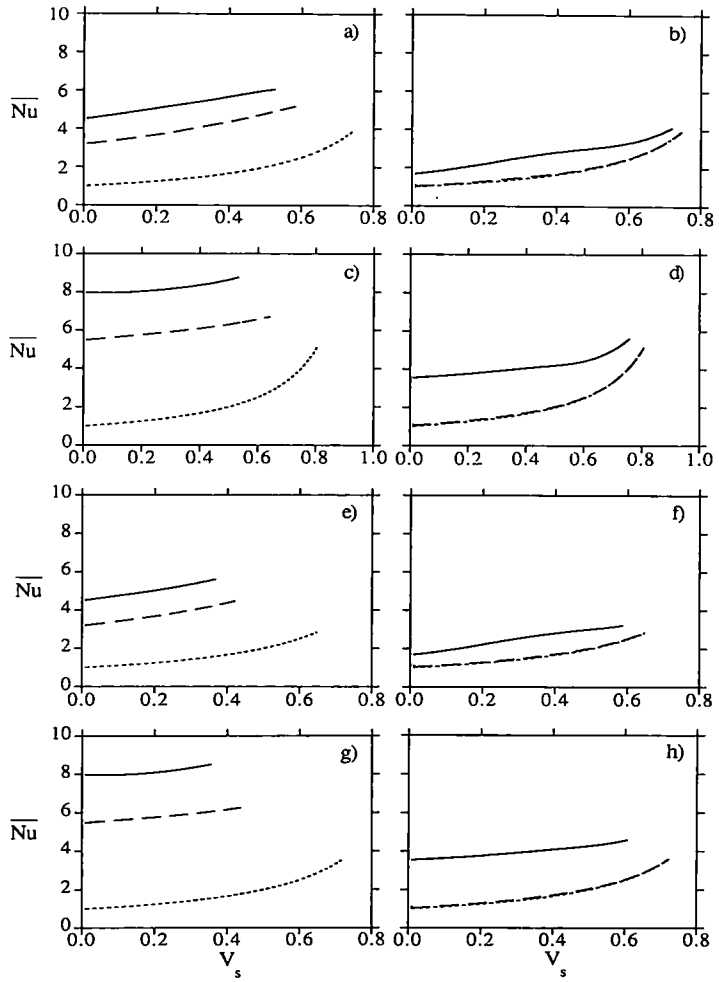

FIG. 11. Predicted $\overline{Nu}$ histories during solidification. Predictions in the left panel correspond to $Bo = 22.7$ while those in the right are for $Bo = 1.43$. Low and high solid subcooling predictions are in the top and bottom halves of the figure, respectively. Predictions for silicon are included in (a), (b), (e) and (f). Sodium nitrate predictions are shown in (c), (d), (g) and (h). The distributions are for the conduction solution (short dashed line), the no-slip simulation (large dashed line) and the thermocapillary simulation (solid line).

ing the melting and solidification cases considered here, thermocapillary effects are deemed significant in each solidification simulation, regardless of Pr, Bo or S_T.

Predicted $\overline{Nu}$ histories during solidification are included in Fig. 11. Again, $\overline{Nu}$ is reported for the conduction solution as well as for $Ma_c = 0, \infty$ cases. In contrast to the results of Fig. 7 (especially, Figs. 7(a) and (b)), thermocapillary effects consistently and significantly increase overall liquid phase convective heat transfer rates and, in turn, decrease overall solidification rates relative to the $Ma_c \approx \infty$ case.

SUMMARY AND CONCLUSIONS

Solidification and melting of low and moderate Pr materials, with the limiting cases of no-slip or thermocapillary boundary conditions applied to the liquid phase, has been considered. Thermocapillary forces are significant in modifying liquid phase convection and heat transfer at low Bo, since heat transfer rates with effective no-slip conditions applied are conduction dominated. High Bo convection is affected by thermocapillarity at the local level.

Local phase change rates are affected significantly, regardless of Bo or Pr. In low Pr materials, enhancements and reductions in Nu are partially offset, leading to overall melting rates which are relatively insensitive to thermocapillary phenomena. Overall sodium nitrate melting rates are increased by thermocapillary convection. Local solidification rates are reduced everywhere by thermocapillary effects regardless of Pr, since (i) the relatively large liquid domains allow propagation of thermocapillary-affected convection to lower regions of the liquid domain and (ii) solid phase conduction desensitizes the response to highly variable Nu.

It is noted that the experiments and simulations were performed under highly controlled, idealized conditions and extension of the results obtained here to practical systems requires caution. In reality, the major challenge is to determine the degree to which solutocapillary effects are present within the system. This is not a trivial task, with nearly all liquid free surfaces being chemically active at the molecular scale. Regardless of the uncertainty associated with surface effects, however, the actual phase change behavior is likely to be bracketed by the limiting cases represented by the effective no-slip and pure thermocapillary treatment of the liquid surface boundary condition.

Acknowledgements—This research was sponsored by NSF Grant CBT-8552806. The authors are grateful for a software development grant from the IBM Corporation.

REFERENCES

1. M. M. Chen, Thermocapillary convection in materials processing. In *Interdisciplinary Issues in Materials Processing and Manufacturing* (Edited by S. K. Samanta, R. Komanduri, R. McMiiking, M. M. Chen and A. Tseng), Vol. 2, pp. 541–558. ASME, New York (1987).
2. S. Davis, Thermocapillary instabilities, *Ann. Rev. Fluid Mech.* **19,** 403–435 (1987).
3. J.-C. Chen, W.-C. Chen and F.-S. Hwu, Numerical computations of unsteady thermocapillary convection in a rectangular cavity with surface deformation. In *Heat Transfer in Metals and Containerless Processing* (Edited by T. L. Bergman, D. A. Zumbrunnen, Y. Bayazitoglu and A. G. Lavine), HTD-Vol. 162, pp. 89–95. ASME, New York (1991).
4. S. Ostrach, Fluid mechanics in crystal growth—The 1982 Freeman Scholar Lecture, *J. Fluids Engng* **105,** 5–20 (1983).
5. T. L. Bergman and B. W. Webb, Simulation of pure metal melting with buoyancy and surface tension forces in the liquid phase, *Int. J. Heat Mass Transfer* **33,** 139–149 (1990).
6. M. Lacroix, Effects of buoyancy and surface tension forces on the melting of a metal, *Numer. Heat Transfer A* **19,** 101–115 (1991).
7. D. Schwabe and A. Scharmann, Some evidence for the existence and magnitude of a critical Marangoni number for the onset of oscillatory flow in crystal growth melts, *J. Crystal Growth* **46,** 125–131 (1979).
8. D. Schwabe and A. Scharmann, Marangoni convection in open boat and crucible, *J. Crystal Growth* **52,** 435–449 (1981).
9. J. R. Keller and T. L. Bergman, Thermosolutal inducement of no-slip boundary conditions in combined thermocapillary-buoyancy cavity flows, *J. Heat Transfer* **112,** 363–369 (1990).
10. C. Beckermann and R. Viskanta, Effect of solid subcooling on natural convection melting of a pure metal, *J. Heat Transfer* **111,** 416–424 (1989).
11. T. E. Voth, The effect of buoyancy and surface tension driven convection on melting of a pure material, M.S. Thesis, The University of Texas at Austin (1992).
12. A. Liu, Solidification of pure materials with liquid phase surface tension effects, M.S. Thesis, The University of Texas at Austin (1992).
13. T. E. Voth, A. Liu and T. L. Bergman, Thermocapillary convection during solid–liquid phase change, *J. Heat Transfer* (in press).
14. D. Schwabe, A. Scharmann, F. Preisser and R. Oeder, Experiments on surface tension driven flow in floating zone melting, *J. Crystal Growth* **43,** 305–312 (1978).
15. T. Daubert and R. Danner, *Physical and Thermodynamic Properties of Pure Chemicals*. Hemisphere, Washington, DC (1989).
16. G. Janz, C. Allen, N. Bansal, R. Murphy and R. Tomkins, *Physical Properties Data Compilations Relevant to Energy Storage*. U.S. Dept. of Commerce, National Bureau of Standards, Washington, DC (1979).
17. S. Hardy, Surface tension of liquid silicon, *J. Crystal Growth* **69,** 456–460 (1984).
18. S. R. Lamphman and T. B. Zorc (Editors), *Metals Handbook*, 10th Edn, Vol. 2. ASM (1990).
19. A. Gadgil and D. Gobin, Analysis of two-dimensional melting in rectangular enclosures in the presence of convection, *J. Heat Transfer* **106,** 20–26 (1984).